Bioinspiration & Biomimetics



RECEIVED 19 February 2018

REVISED 8 June 2018

ACCEPTED FOR PUBLICATION
18 June 2018

PUBLISHED 20 July 2018 **PAPER**

Swimming performance of a bio-inspired robotic vessel with undulating fin propulsion

Hanlin Liu and Oscar Curet®

Ocean and Mechanical Engineering, Florida Atlantic University, Boca Raton, FL 33431, United States of America E-mail: ocuret@fau.edu

Keywords: bio-inspired propulsion, underwater vehicles, biomimetics, fish swimming, fluid dynamics, undulating fins Supplementary material for this article is available online

Abstract

Undulatory fin propulsion exhibits a high degree of maneuver control—an ideal feature for underwater vessels exploring complex environments. In this work, we developed and tested a selfcontained, free-swimming robot with a single undulating fin running along the length of the robot, which controls both forward motion and directional maneuvers. We successfully replicated several maneuvers including forward swimming, reversed motion, diving, station-keeping and vertical swimming. For each maneuver, a series of experiments was performed as a function of fin frequency, wavelength and traveling wave direction to measure swimming velocities, orientation angles and mean power consumption. In addition, 3D flow fields were measured during forward swimming and station-keeping using volumetric particle image velocimetry (PIV). The efficiency for forward swimming was compared using three metrics: cost of transport, wave efficiency and Strouhal number (St). The results indicate that the cost of transport exhibits a V-shape trend with the minimum value at low swimming velocity. The robot reaches optimal wave efficiency and locomotor performance at a range of 0.2–0.4 St. Volumetric PIV data reveal the shed of vortex tubes generated by the fin during forward swimming and station keeping. For forward swimming, a series of vortex tubes are shed off the fin edge with a lateral and downward direction with respect to the longitudinal axis of the fin. For station keeping, flow measurements suggest that the vortex tubes are shed at the mid-section of the fin while the posterior and anterior segment of the vortex stay attached to the fin. These results agree with the previous vortex structures based on simulations and 2D PIV. The development of this vessel with high maneuverability and station keeping performance has applications for oceanography, coastal exploration, defense, the oil industry and other marine industries where operations are unsafe or impractical for divers or human-piloted vessels.

Introduction

Autonomous underwater vehicles (AUVs) are critical in the performance of underwater missions, including ocean exploration, inspection of coastal structures and shipwrecks, as well as in defense [1, 2]. Despite the capabilities of current AUVs, they have limitations in terms of performing precise station keeping in the presence of currents as well as other external forces that could otherwise result in vehicles drifting out of position. In addition, current AUVs exhibit limited maneuverability, which restricts their performance in complex environments such as turbulent surf zones [3]. At low speeds, the efficiency of propellers to generate thrust declines considerably

making it difficult for these propeller-driven vehicles to maneuver or hover in place [4]. Fish are able to achieve high efficiency and impressive maneuvers that far exceed conventional man-made vehicles. Thus, bio-inspired propulsors could be a solution to the challenges of low-speed maneuvering and station keeping [5]. In this work, we present a novel bio-inspired underwater robot—the *KnifeBot*—that controls forward motion and directional maneuvers, undulating a single fin that runs along the ventral side of the vessel.

Fish locomotion using ribbon-fin propulsion has evolved independently for various ray-finned fishes in marine and fresh water, providing rich fin morphology variations [6,7]. In this type of swimming mode,

aquatic organisms generate thrust by sending traveling waves along one or multiple fins. The fins can be located at the dorsal side (e.g. amiiform), the ventral side (e.g. gymnotiform) or a combination of both (e.g. balistiform). These swimmers are capable of modulating different traveling waves along the fins to adjust to various flow conditions, thus achieving remarkable maneuvers and swimming efficiently at low speeds [8,9].

The American knifefish is an example that uses this type of undulating fin propulsion (figure 1(A)). The fish has a low aspect ratio fin that runs along the ventral midline. The fin is composed of more than a hundred bony rays that are interconnected with a collagen membrane [10, 11]. During forward swimming, the fish keeps its body mainly straight and uses the fin as the main propulsor. Moreover, the fish can perform impressive changes in direction including rapid breaks, precise station keeping and alternate between forward and backward motion changing the kinematics of the undulating fin [12–19]. These outstanding maneuvers make this propulsion method of particular interest for underwater vehicles.

The motivations of the present study are as follows. First, the aim is to understand the swimming performance and maneuver control of undulating fin propulsion; second, to understand the 3D fluid dynamics associated with this propulsion method. The knowledge gained through this research can provide promising insight into the design, development and design of highly maneuverable underwater vessels for applications such as ocean exploration, underwater rescue and coastal structures inspections [3].

Different approaches have been used in previous studies to understand undulating fin-based propulsion, including live animal observation [6, 11, 18, 20], theoretical/numerical analyses [21–27], as well as physical models [28-44]. Numerous robotic devices have been developed to study undulating fin propulsion. The design complexity, fabrication and control of these robotic platforms can vary enormously. Lauder et al [28] used a simple robotic flapping foil apparatus to explore the effect of actuation parameters on the locomotor characteristics. Liu et al [43] developed a ribbon-fin model to investigate the effect of fin ray stiffness and fin morphology on the thrust generation, power consumption and propulsive efficiency of ribbon-fin propulsion with flexible rays. Although these simple physical models could fulfill some important research questions, robotic devices with the control of each individual ray allow the study of undulating fin propulsion with a much broader range of actuation parameters [18, 19, 32, 37, 39, 42]. For instance, Epstein et al [32] constructed a robotic device of a ribbon fin composed of eight rays, actuated individually, linked by a thin latex sheet to measure the thrust force with changing actuation parameters (frequency, amplitude and wavelength). Curet et al [19, 39] used a robotic undulating fin model, Ghost-Bot, composed of 32 rays covered by a Lycra membrane to study propulsive force, swimming velocity and flow structures generated by the undulating fin. The robotic device housed 32 motors in a spiral overlapping arrangement inside the torpedo-like hull. This robot has to be mounted and tethered to receive power and signals outside the water. Neveln *et al* used a similar physical model to conduct flow measurements around the undulating fin [42].

Previous experimental studies mainly focused on the fin kinematics, hydrodynamics and thrust generation of undulatory fin propulsion. However, the potential of using a single undulating fin to control the six-degree of freedom of an underwater vessel has remained elusive. As a first step toward the 3D motion control of vessels propelled by undulating fins, we focused on the kinematics and performance of three key maneuvers: forward swimming, reversed motion and station keeping (figure 1(B)). In addition, we demonstrated the ability of vertical swimming. For forward swimming, three metrics of swimming performance are presented: cost of transport (COT), wave efficiency and Strouhal number.

Some key parameters used throughout the paper are displayed in the schematic diagrams (figures 1(C) and (D)). The Eulerian reference frame is presented as x, y, z and the robot body frame is given by X (surge), Y (sway) and Z (heave). Traveling waves initiated from the leading edge of the ribbon fin (anterior part) and proceeding to the trailing edge (posterior part) are defined as the 'head waves'. Those from the opposite direction (trailing edge to leading edge) are termed 'tail waves'. The Euler orientation angles, (Φ_x, Φ_y, Φ_z) , are roll, pitch, and yaw, respectively. θ is the angle deflection of the fin (the maximum deflection amplitude is θ_{max}). λ is the traveling wavelength. $L_{\rm fin}$ represents the fin length. The 'number of undulations' is defined as L_{fin}/λ , the reciprocal of the specific wavelength [8, 45]. The height of the fin and the body are given by h_{fin} and h_{body} respectively. Points **B** and **Cg** denote the center of buoyancy and center of gravity, respectively. The net force generated by the undulatory fin is given by $F_{\text{fin net}}$ which can be divided into the X-axis component F_{finX} and in Z-axis F_{finZ} . The mean lateral force F_{finY} is equal to zero over one fin cycle. The drag of the vessel is given by F_{drag} .

A series of experiments were conducted to measure the vessel's kinematics and mean power consumption during forward swimming, reversed swimming and hovering (see supplementary material movies 1–5 (stacks.iop.org/BB/13/056006/mmedia)). For each experimental set, we measured free-swimming velocities, power consumption and orientation angles of the robot. The evolution of the flow structures for forward swimming and station-keeping are shown in supplementary movies 6 and 7, respectively.

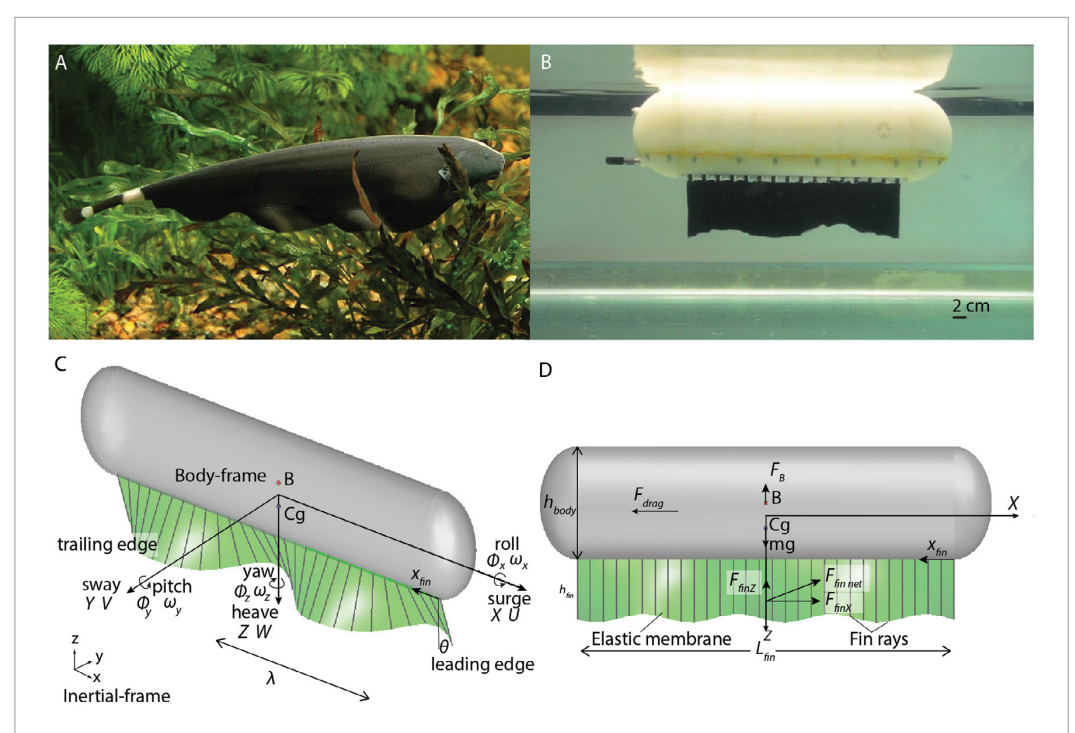


Figure 1. Photograph of black ghost knifefish, the *KnifeBot* and schematic of the robotic model. (A) *Apteronotus albifrons* from South America (photo courtesy of Per Erik Sviland). Typical adult fish measure from 15 cm to 50 cm. (B) Snapshot of the robotic vessel swimming in the water tank. (C) Schematic of the robotic model from perspective view showing the inertial reference frame (x,y,z); the robot body frame (X,Y,Z); the orientation Euler angles (Φ_x,Φ_y,Φ_z) ; the wavelength (λ) and angular fin deflection (θ) of the traveling wave. The center of gravity and buoyancy are presented as $C\mathbf{g}$ and \mathbf{B} respectively. (D) Schematic of the model from lateral view displaying the height of the fin h_{fin} , the height of the body h_{body} , the fin length L_{fin} , the drag force F_{drag} , the net force generated by the undulatory fin F_{fin} net with its component in the X direction $F_{\text{fin}X}$ and Z direction $F_{\text{fin}Z}$. X_{fin} is the reference frame along the pivot axis of the fin to prescribe the kinematics of the fin.

Materials and methods

Robotic vessel model: the KnifeBot

The overall design of the *KnifeBot* (figure 2(A)) consists of the mechanical configuration (including hull construction and power transmission) and the electronics (including motor control, sensors and data acquisition).

The robot features a compact slender body with an oval-shaped cross-section and one semi-ellipsoid cap at each end. Its overall length is 46.2 cm; the width is 7.7 cm and the height is 12.5 cm without the fin part. The fin is 30 cm long and 7 cm high ($L_{\text{fin}} = 30 \text{ cm}$; $h_{\rm fin} = 7$ cm). The hull is composed of two parts: the upper shell and the bottom support. The upper shell and bottom support were divided into five segments, which were manufactured via a 3D printer. The hull houses one master board, four slave boards to control the motion of the motors, and the sensors (figure 2(C)). The batteries (Li-ion 18650) are located in the semi-ellipsoid caps. The robot houses sixteen motor units (RE10, Maxon Motor AG, Sachsein, Switzerland) along the centerline of the bottom support with a constant spacing distance of 2 cm. Each motor unit includes a motor, a 64:1 gear reducer and a two-channel encoder with 16 counts per motor rotation. A connector (Impulse IE55-1206-BCR) was installed in the trailing end of the bottom support (figure 2(D)) to recharge the batteries and to transfer data. On the external side of the upper hull, a vacuum plug was fitted at the trailing end to control the pressure of the inner room. In addition, we designed mountings to install pectoral fins for future studies.

Stainless steel shaft collars were used to water-proof the rotational output of the motor to the rays. Rotary shaft seals (13125K64 McMaster-Carr) were used to reduce the rotational friction (figure 2(B)). Note that all motors were placed in a vertical orientation. 90° bevel gears were used to transmit the vertical rotational motion of the motor to the lateral motion of the rays. A Buna-N rubber o-ring (4464T323 McMaster-Carr) with an A65 durometer was used to waterproof the interface between the upper shell and the bottom support. Twenty screws were used to hold the two parts.

The center of gravity was designed to be below the center of buoyancy to ensure the stability of the vessel. The robot was designed to be slightly negative buoyant in a similar fashion to the knifefish [19]. When the robot was submerged into the water without actuation, it would sink to the bottom of the tank slowly. In addition, the fore body part was designed to be slightly heavier than the aft body with an initial negative pitch angle of approximately -1.2° .

The *KnifeBot* is a self-contained system that contains all the electronic components, including four

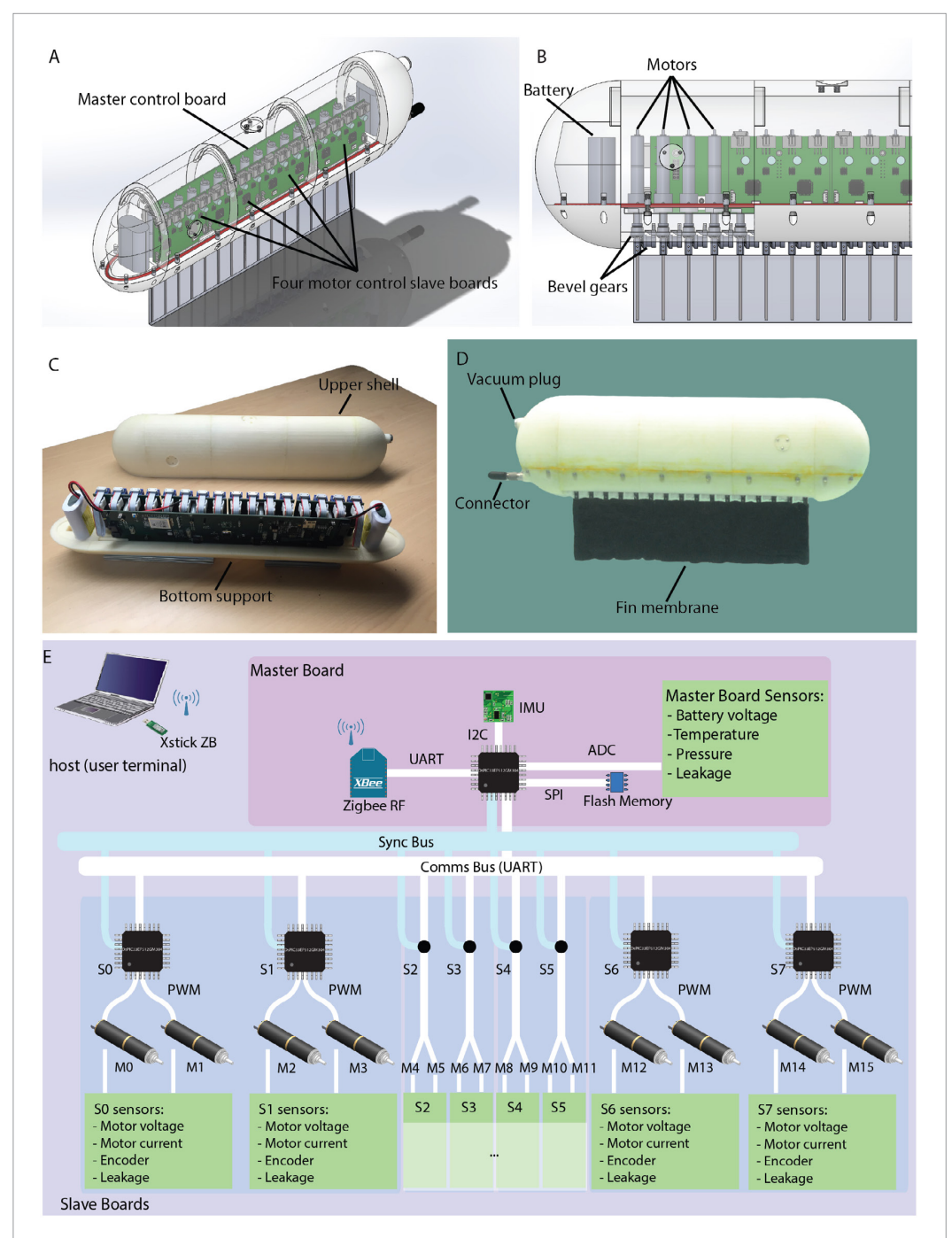


Figure 2. Robot mechanism and electronic architecture of the KnifeBot. (A) Overall design schematic of the robotic device. (B) Close-up view of a body section to illustrate the power transmission mechanism. (C) Photograph of the upper shell, bottom support and onboard electronic components. (D) Photograph of the integrated robot including the hull and the fin membrane attached to it. (E) Electronic architecture of the robot to elucidate the functionality and structural connection of the electronic components on the master board and four slave boards.

motor control boards (slave boards), one master control board, batteries and motors inside the hull (figure 2(E)). Each slave board hosts two microcontroller units (MCUs) (dsPIC33EP512GM304, Microchip Technology) to control the four motors via pulsewidth modulation (PWM). As the ribbon fin performs the undulatory kinematics, each ray/motor undergoes a sinusoidal oscillating motion. A proportional-

integral-derivative (PID) controller was implemented to control the position of the motors. A sine look-up table with 256 values was established for the sinusoidal motion of the motor positions in one cycle. At each time step, the MCU obtains the angular position of the motor from the encoder as the feedback input and reads the next position value from the look-up table as the setpoint. The PID module outputs a corrected

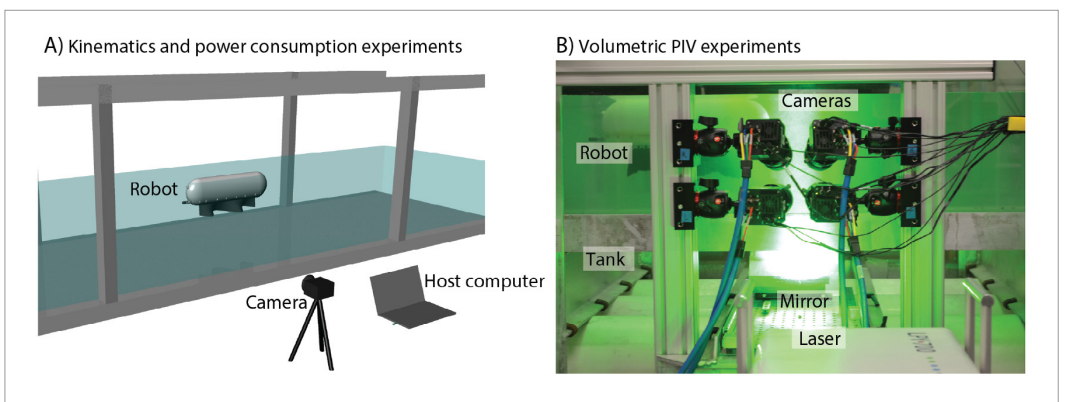


Figure 3. Free-swimming experimental setup and volumetric particle image velocimetry (V3V PIV). (A) The schematic diagram of experimental setup to measure swimming velocities, orientation angles and power consumption. The robot was launched manually in a wave tank along the centerline to perform different maneuvers. (B) V3V PIV configuration. Four synchronized cameras were mounted on an aluminum frame, pointing to the tank. A mirror was placed under the tank to deflect the laser volume emitted from the laser head.

PWM signal to control the motor speed. Simultaneously, the slave microcontrollers measure the voltage and current of the motors to calculate the power consumption.

The master control board accommodates one microcontroller for implementing multiple functionalities. First, it sets up a Sync Bus to synchronize the time line for all slave MCUs, and the actuation of each motor. Second, the master establishes a Comms Bus through an universal asynchronous receiver transmitter (UART) module to communicate with all the slaves. Once the master MCU receives an instruction from the host, it transmits the message to all slave MCUs via the Comms Bus. In addition, the slave boards can send the motor power and position data back to the master board. The master MCU interfaces with the other electronic components. For instance, it connects a Zigbee radio frequency module through the UART peripheral to communicate with the computer host (laptop computer). Although a radio signal is not suitable for deep-water communication, it was adequate for the water level and tests performed in this study (~0.6 m depth). During operation, the host computer transmits a control command via the radio signal, containing information about the motion pattern (forward swimming, reversed swimming or hovering motion), the undulating frequency (0.5, 1.0, 1.5, 2.0 2.5, or 3.0 Hz) and number of undulations (one or two) along the fin. For the current number of actuators, which is 16, we can resolve a reasonable two undulations along the fin. An inertial measurement unit component (PNI M&M module) is used to measure the linear acceleration (a_x, a_y, a_z) , Euler angles of the robot (roll Φ_x , pitch Φ_v , yaw Φ_z) and rotational velocity $(\omega_x, \omega_v, \omega_z)$ through inter-integrated circuit (I²C) protocol. A 16 MB flash memory (Winbond's W25Q SpiFlash) unit is connected to the master MCU via a serial peripheral interface (SPI) to save all the collected data. In addition, the master MCU interfaces with various sensors including temperature, pressure and leakage sensors through an analog-to-digital converter (ADC) module

allowing the operator to monitor the inner pressure/temperature and leakage.

Fabrication of the robotic hull and the fin part

The hull segments were fabricated with ABS*plus* using a Mojo Desktop 3D printer (Stratasys Corp.) with a vertical resolution of 0.178 mm (printing resolution). Due to the limitation of the printing space (12.7 cm \times 12.7 cm \times 12.7 cm), the upper shell and bottom support were printed in five sections. After printing, an epoxy (BJB TC-1614) was used to seal the 3D printed parts [55]. Subsequently, all the upper and bottom sections were assembled and bonded together.

The membrane of the fin was composed of a double layer Lycra fabric. Previous ribbon-fin models have used various materials to make the fin membranes, which can cover a large range of mechanical properties. Low [36] used rigid acrylic segments as the fin—a considerable departure from flexible ribbon fins. Other options include elastic rubber or fabric, such as a Latex sheet [18, 32] or Lycra membrane [19, 39] with a Young's modulus of 0.2 MPa, similar to the fish fin membrane [56]. The rays to actuate and manipulate the membrane were composed of Delrin Actural Resin ($EI = 2.32 \times 10^{-3}$) Nm² with a 7 cm high and approximately 0.1 cm width, as used in a previous study regarding the stiffness of fin rays [43]. The distance between two proximal rays is 2 cm. From a biological standpoint, fish fin rays are highly flexible and can exhibit substantial bending during swimming [11].

Experimental procedures

A series of free-swimming experiments were performed in a wave tank of 1.22 m (4 feet) high, 1.22 m (4 feet) wide and 18.29 m (60 feet) (figure 3(A)). For the experiments the water depth was approximately 0.6 m. The vehicle was launched by an operator at the centerline of the tank. The robot was controlled remotely using a laptop computer. A camera with 1920×1080 pixel resolution was used to record the

movement of the robot from the lateral perspective or bottom view.

Three series of experiments were performed to study forward swimming, reversed swimming and hovering. In forward swimming, the undulating frequency was varied from 0.5 Hz to 3.0 Hz with a step of 0.5 Hz and number of undulations from 1 to 2. For each trail, kinematics and mean power data were collected for approximately a travel distance of 3.66 m. The kinematics were recorded with a camera at 24 frames per second (fps) after swimming 1.22 m and the robot had passed the acceleration phase and reached a quasi-steady state swimming state. During reversed swimming, the robot swam forward for almost 2.44 m, then a reversed command was transmitted. With the reverse command the traveling wave started to propagate in the opposite direction (from the tail to head). The reverse maneuver was tested for 1.0 Hz and 2.0 Hz with one undulation. In the last experimental set, the undulating fin had counterpropagating waves—one traveling wave from the head and one wave from the tail. With these fin kinematics the robot was able to initially perform vertical swimming. Then, the robotic fish reached the water surface since the heave force generated by the fin was larger than the result of the buoyancy minus the weight. At the surface, the robotic device was able to hover. The counter-propagating waves' kinematics were tested for 1 and 2 Hz. All the free-swimming kinematics of the vessel were analyzed using a MATLAB® (version R2014b; Mathworks®) program. The black plug at the rear of the vessel was used to track the vessel motion using image processing through MAT-LAB®. The length of the vessel was used to convert pixels to meters. For the data processed, the robotic fish was traveling parallel to the longitudinal axis of the water tank.

The motor power consumption and robot orientation were measured with sensors inside the vessel. These measurements were recorded after the command signal to initiate the fin undulation. The data were collected 16 times per cycle. For instance, when the fin was actuated at 2.0 Hz, these measurements would be written into the flash memory at a frequency of 32 Hz. To analyze the results' varying frequency, we took the mean value of the time evolution data at each frequency after the first several undulating cycles to minimize the effect of the initial perturbation introduced by the hand launch.

The configuration of the flow measurement using volumetric PIV is shown in figure 3(B). Four synchronized cameras (Powerview Plus 12Mp-180) were mounted on an aluminum frame and used to capture the wake features generated by the robot. The cameras were calibrated across the full spatial field of view using Insight V3V 4G software (TSI, Shoreview, MN, USA) with a calibration target of an even spacing grid. The volume of the flow measurements was $60\,\mathrm{mm}$ (length) \times $80\,\mathrm{mm}$ (height) \times $40\,\mathrm{mm}$ (width)

and the images were captured with a pixel resolution of 4096×3072 . After image post-processing, MATLAB® was used to plot the flow fields.

Results

Forward swimming

By sending head waves from the leading edge to the trailing edge of the fin, the robot generates a propulsive force to swim forward. An idealized sinusoidal wave along the fin was implemented using the following equation:

$$\theta_{ray}(x_{fin}, t) = \theta_{max} \sin \left[2\pi \left(\frac{x_{fin}}{\lambda} + ft \right) \right]$$
 (1)

where x_{fin} is the fin coordinate along the longitudinal axis (figure 1(D)); t is the time; θ_{max} is the maximum angular deflection (deflection amplitude) from the midsagittal plane, which was set as 30° in the experiments; λ is the wavelength and f is the undulating frequency. Movies S1–S3 in the supplementary material show the forward swimming from the side and bottom views, respectively. Snapshots of the motion of vessels are shown in figure 4 for fin frequencies of 0.5 Hz, 1.0 Hz and 3.0 Hz with one undulation (figures 4(A)–(C)) and two undulations (figures 4(D)–(F)). The arrows indicate the trajectory and velocity of the robot during forward swimming. The velocity vectors are colored by the velocity magnitude. As can be observed, the robot can achieve higher swimming velocity as the frequency increases for a given wavelength. Thus, the robot can travel farther distance after for a specific time (2.0 s). Through a comparison of the cases under the same frequency with a different number of undulations, the robot exhibits a lower swimming velocity with two undulations along the fin.

From figures 4(A)–(C), the robot with one undulation along the fin swam at the water surface with a fairly constant swimming velocity, indicating that the undulatory ribbon fin with head traveling waves can generate a thrust force in the surge direction as well as an upward force in the heave direction to overcome the submerge weight $(F_B - mg)$ of the robot. However, for two undulation and 0.5 Hz (figure 4(D)), the heave force is smaller than the resultant submerge weight, resulting in the robot device swimming close to the bottom wall of the tank. For 1 Hz and two undulations (figure 4(F)), the robot device exhibits a diving trajectory, indicating that the heave force is slightly smaller than the submerge weight of the robot. The robotic device swims at the surface at a fin frequency of 3 Hz and two undulations (figure 4(F)) indicating that the heave force surpassed the submerged weight.

Figure 5 shows the swimming velocity and orientation angle as a function of fin frequency. The symbols are color-coded by the frequency. Filled and open symbols represent the results with one undulation and two undulations along the fin, respectively. In figure 5(A), the swimming velocity increases with frequency.

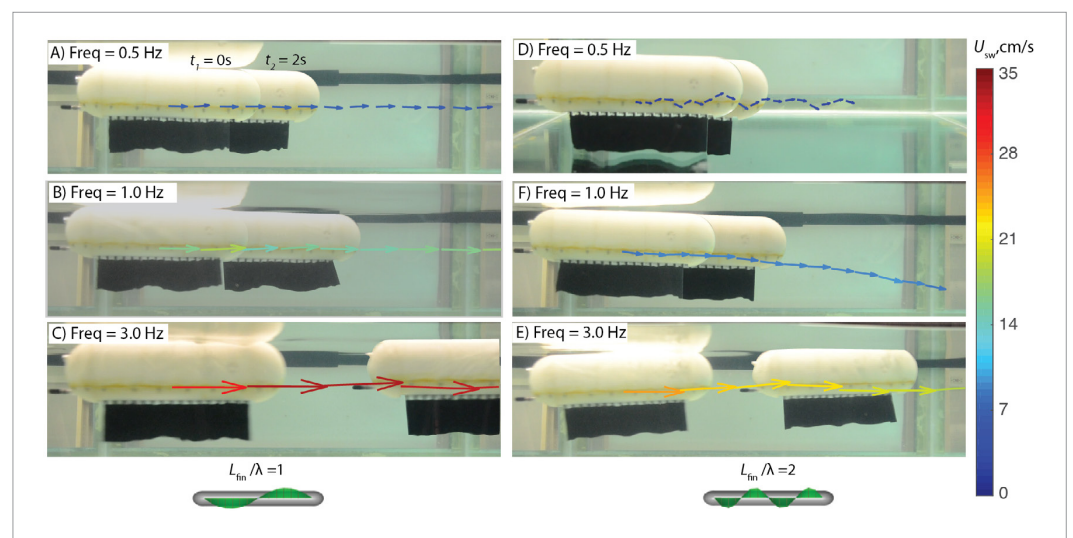


Figure 4. Snapshots of robot forward swimming with the trajectories and velocity vectors shown. (A)–(C) Forward swimming cases with selected frequencies (f = 0.5, 1.0 and 3 Hz), with one undulation along the fin, $L_{\text{fin}}/\lambda = 1$. See supplementary material movie S1 for corresponding video. (D)–(F) Forward swimming scenarios with two undulations, $L_{\text{fin}}/\lambda = 2$, under the same frequencies. See supplementary material movie S2 for the corresponding video. In each snapshot, the robot appears twice to show its position after 2 s. The color map from dark blue to dark red indicates the magnitude of velocity vectors from 0 to 35 cm s⁻¹.

At the same frequency, the robot with a higher number of undulations exhibits a lower velocity. The inset shows the time evolution of surge displacement exemplified by the swimming cases of 1.0 Hz and 3.0 Hz. For each frequency, it exhibits a highly linear relationship between the surge displacement and the time, indicating that the swimming velocity is constant and the robot reached a quasi-steady swimming state.

Figure 5(B) shows that the mean pitch angle of the robot also increases with the frequency and decays with the number of undulations. Note that the case with f = 0.5 Hz and $L_{\rm fin}/\lambda = 2$ displays a large standard deviation because the robot was swimming in contact with the bottom of the tank, causing a significant effect on the pitch angle. The inset shows how the pitch angle varies with time at 1.0 Hz and 3.0 Hz. We observe that the vessel exhibits a periodic oscillation whose frequency and amplitude both increase with frequency. Figures 5(C) and (D) present the roll and yaw angles as functions of frequency. The roll and yaw angles are both distributed along 0°, however the roll angles present smaller standard deviations. The timeevolution of roll and yaw angles (insets of figures 5(C) and (D)) show an oscillation amplitude within the range of $\pm 10^{\circ}$. It can be observed that as the number of undulations increases, the standard deviations of swimming velocity and orientation angles reduce. This suggests that the robot has a higher stability with a larger number of undulations.

In the forward swimming case, the data show that the free-swimming velocity increases with frequency, which is as expected because the propulsive force generated by the undulatory fin grows with the frequency [32, 39, 43]. However, unlike the thrust force that exhibits an exponential relationship with the frequency, the free-swimming velocity increases lin-

early at low frequencies. At higher frequency, the rate at which the swimming velocity increases tends to decrease.

Figure 6(A) shows the swimming velocity as a function of wave speed V_{wave} . Note that the swimming velocity exhibits a fairly uniform trend with wave speed regardless of the number of undulations along the fin. At the same wave speed, the case with two undulations can even reach a slightly higher swimming velocity. The total mean power consumption of the motors is shown in figure 6(B).

The Strouhal number (St) is broadly used as an important non-dimensional number to characterize unsteady oscillating flow in the wake of fish locomotion [42,46], expressed as:

$$St = \frac{fA}{U_{\text{sw}}} \tag{2}$$

where f is the fin actuation frequency, A is a characteristic length associated with the oscillation and U_{sw} is the swimming velocity. In this study the characteristic length was defined as the mean peak-to-peak amplitude at the mid-fin height. The Strouhal number of the robotic device as a function of the swimming velocity is shown in figure 6(C). For one undulation the minimum St is approximately 0.2 and for two undulations the minimum St is approximately 0.4. This range of Strouhal number is in agreement with the Strouhal number found in swimming and flying animals [47]. St represents the ratio of local inertial force to the convective inertial force. For fish locomotion, St indicates the ratio of local momentum input from the fin to the wake to the output momentum exerted on the fish from the wake to moving the fish forward [42]. St has been used to characterize propulsion force and the efficiency of

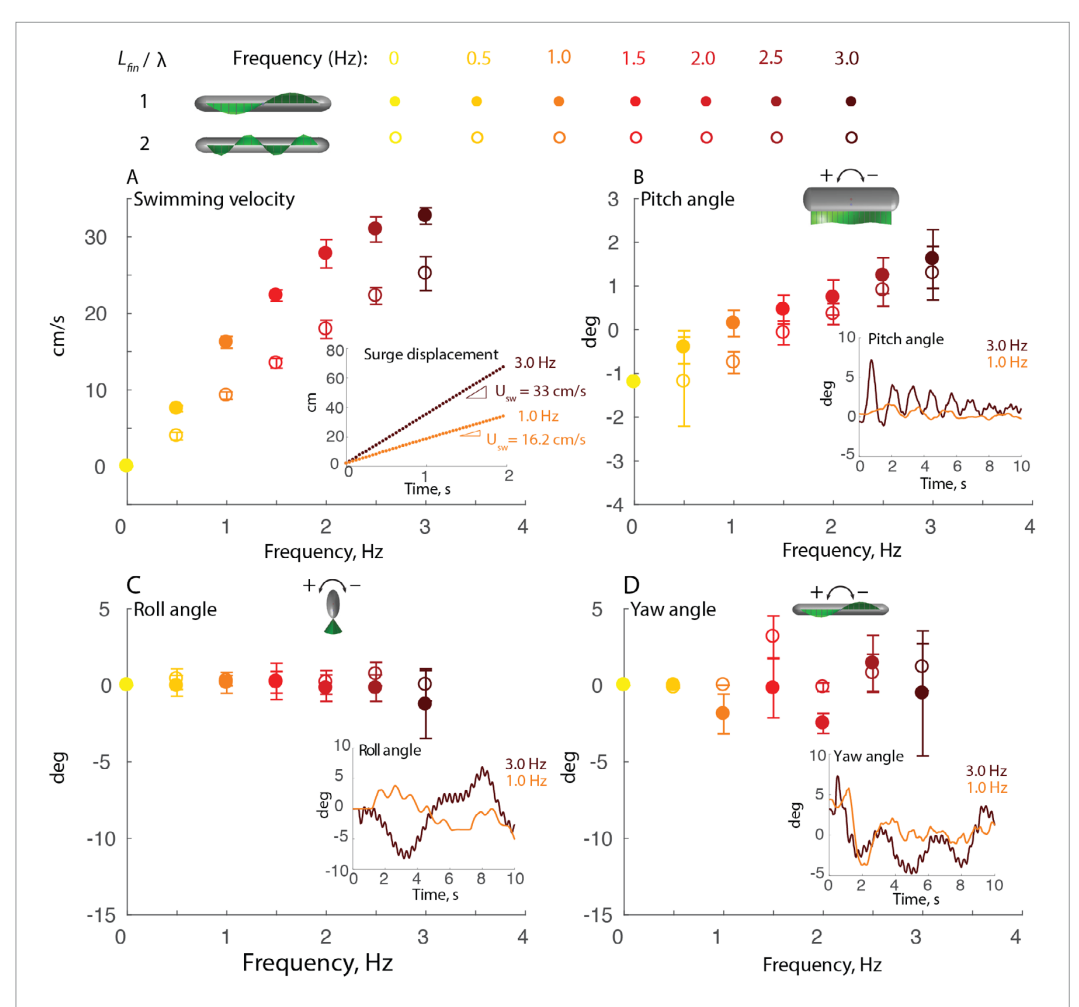


Figure 5. Experimental results of forward swimming as functions of frequency. (A) Swimming velocity as a function of frequency. The inset shows the surge displacement versus time at $1.0\,\mathrm{Hz}$ (in orange color) and $3.0\,\mathrm{Hz}$ (in brown color) with one undulation along the fin. (B)–(D) Euler angles of pitch roll and yaw against frequency respectively. In each panel, the inset displays the time evolution of the corresponding orientation at $1.0\,\mathrm{Hz}$ and $3.0\,\mathrm{Hz}$ with one undulation. Frequencies from low to high are color-coded from yellow to brown. Error bars represent the standard deviations.

oscillating and undulating locomotion. The *St* range of 0.2–0.4 in combination with specific kinematics (A/L = 0.1-0.3) results in optimal swimming [57].

Another indirect measure of swimming efficiency is wave efficiency [48] or slip [49], defined as the ratio of swimming velocity to traveling wave speed:

$$\eta_{wave} = \frac{U_{\rm sw}}{V_{wave}} \tag{3}$$

where V_{wave} is the traveling wave velocity. η_{wave} has a range between 0 and 1, where $\eta_{wave}=0$ represents no forward motion, and $\eta_{wave}=1$ indicates the swimmer is swimming forward as fast as the traveling wave moves backwards. Figure 6(D) shows the wave efficiency as a function of swimming speed. The wave efficiency ranges from approximately 0.35 to 0.6 depending on the fin actuation parameters. The wave efficiency for *A. albifrons* has been reported to reach as high as 0.7 [18]. Wave efficiency is a practical measure for live animal observation since it is only based on kinematics. However, it has some limitations, as it

does not provide any information on the actual energy consumption during swimming.

A measurement widely used to compare locomotion efficiency is the COT (COT = P/U_{sw}) [50–52]. A lower COT indicates a better performance, as the animal or vessel moves farther with less amount of energy. Figure 6(E) shows the COT of the robotic device during forward swimming. The COT follows a V-shape trend against swimming velocity for both one and two undulations with the best performance (minimum point) for lower swimming velocities. As can be observed, the wave efficiency and COT provide two different optimal actuation parameters (see details in the discussion).

Reversed swimming

In the experiments of reversed maneuver, the robot was initially swimming forward, as shown in figure 7(A). Once a reversal command was sent, the fin rays stopped propagating head waves and started to generate tail waves from the trailing edge. As the robot changes

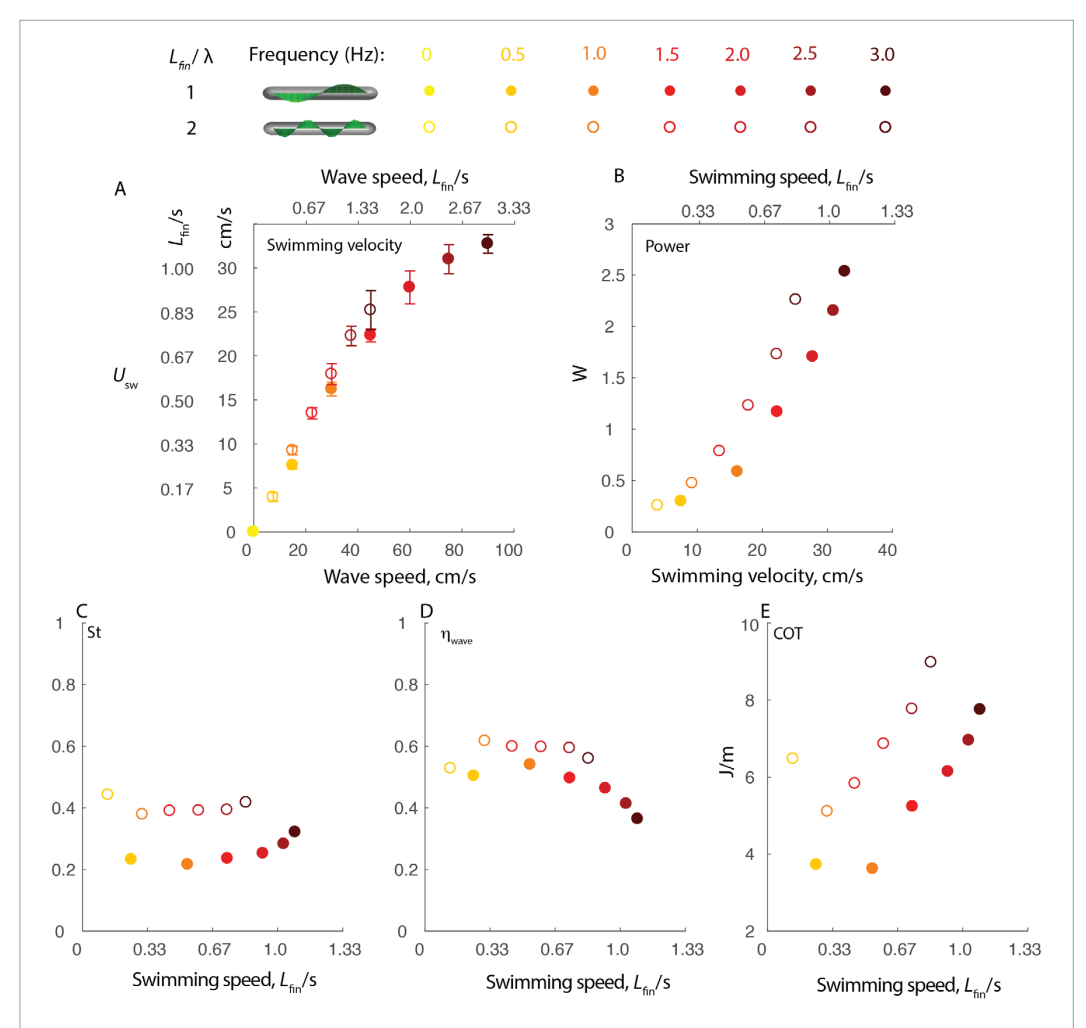


Figure 6. Forward swimming characteristics for different velocities. (A) Swimming velocity as a function of traveling wave speed. (B) Power consumption against swimming velocity. (C)–(E) Strouhal number (St), wave efficiency (η_{wave}) and COT as a function of swimming velocity, respectively.

swimming direction from forward to backward swimming (figures 7(A)–(C)), it also experienced variations in the orientation angle (figures 7(B)–(F)). Movie S4 shows the overall process at 1.0 Hz and 2.0 Hz.

Figure 7(C) shows the time evolution of the swimming velocity from approximately the 10th second to the 25th second. The robot was firstly swimming forward with a mean velocity of 17.2 cm s⁻¹ and a pitch angle of 0.146° (the green regions of figures 7(C) and (E)). After the command was sent, the reversal transition lasted approximately 2 s (the magenta regions in figures 7(C)–(F)) before swimming in the opposite direction with a mean velocity of 11.4 cm s⁻¹ and negative pitch angle of 1.695° (the blue regions of figures 7(C) and (E)). The rapid brake and reversal transition introduced a sharp fluctuation in the Euler angles, denoted as the peak points in the magenta regions.

Hovering maneuver and vertical swimming

The knifefish is able to perform hovering or station-keeping by two counter-propagating waves simultaneously [17, 18]. The opposite traveling waves meet close to the center of the fin length while the fish is hovering [17]. We can simulate similar counter-propagating waves by the summation of two traveling waves as $\theta_{ray} = \theta_1 + \theta_2$, where θ_1 and θ_2 are the angular deflection of the two different waves, one traveling from the leading edge to the trailing edge and other in the opposite direction (see inset figure 8(A)). The angles are given by:

$$\theta_1\left(x_{\text{fin}},t\right) = G_1\left(x_{\text{fin}}\right)\theta_{\text{max}}\sin\left[2\pi\left(\frac{x_{\text{fin}}}{\lambda} + ft\right)\right]$$
(4)

$$\theta_{2}\left(x_{\mathrm{fin}},t\right)=G_{2}\left(x_{\mathrm{fin}}\right)\theta_{\mathrm{max}}\sin\left[2\pi\left(\frac{x_{\mathrm{fin}}}{\lambda}-ft+\phi\right)\right]$$
(5)

where ϕ is the phase lag, set as $\phi = \pi$. $G_1(x_{\text{fin}})$ and $G_2(x_{\text{fin}})$ are shape control functions for θ_1 and

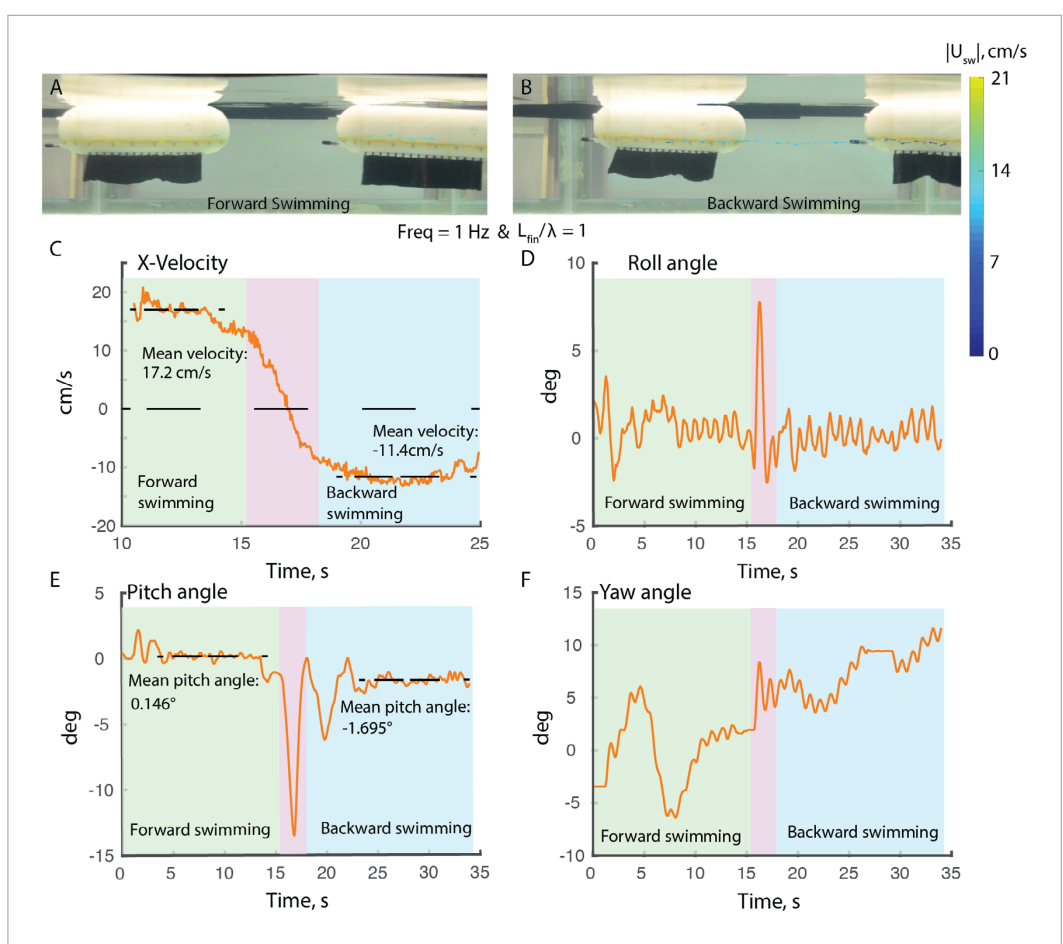


Figure 7. Snapshots of reversed maneuver and the time evolution results of swimming velocity as well as the Euler angles. (A) and (B) Snapshots of the robot swimming forward, undergoing a rapid brake then swimming backwards at a frequency of 1.0 Hz and one undulation along the fin. The velocity vectors are displayed and colored by the magnitude. (C) The time evolution result of swimming velocity. The mean velocity is $17.2~{\rm cm\,s^{-1}}$ for forward swimming part and $-11.4~{\rm cm\,s^{-1}}$ for backward swimming session. (D)–(F) Time evolution results of roll, pitch and yaw respectively. The green region represents the forward motion; the magenta region denotes the rapid brake and reversal transition; the blue region shows the backward swimming. See supplementary material movie S4 for corresponding video.

 θ_2 , respectively. In the current study, they are piecewise functions of the fin position, defined as:

$$G_{1}\left(x_{\text{fin}}\right) = \begin{cases} 0 & x_{\text{fin}} < 0.3L_{\text{fin}} \\ -2.5\frac{x_{\text{fin}}}{L_{\text{fin}}} + 1.75 & 0.3L_{\text{fin}} \leqslant x_{\text{fin}} \leqslant 0.7L_{\text{fin}} \\ 1 & x_{\text{fin}} > 0.7L_{\text{fin}} \end{cases}$$
(6)

$$G_{2}\left(x_{\text{fin}}\right) = \begin{cases} 1 & x_{\text{fin}} < 0.3L_{\text{fin}} \\ 2.5\frac{x_{\text{fin}}}{L_{\text{fin}}} - 0.75 & 0.3L_{\text{fin}} \leqslant x_{\text{fin}} \leqslant 0.7L_{\text{fin}} \\ 0 & x_{\text{fin}} > 0.7L_{\text{fin}} \end{cases}$$

where L_{fin} is the fin length. The shape control functions $G_1(x_{\text{fin}})$ and $G_2(x_{\text{fin}})$ are depicted in the inset of figure 8(A).

Movie S5 in the supplementary material provides a video of vertical swimming first and then the hovering maneuver. The vertical swimming velocity of the robot is approximately $2.5 \, \mathrm{cm \ s^{-1}}$ at $1.0 \, \mathrm{Hz}$, and approximately $8.8 \, \mathrm{cm \ s^{-1}}$ as the frequency turns to $2.0 \, \mathrm{Hz}$. Figure 8(A) shows the fin kinematics of the two counter-propagating waves. The time evolution of

roll, pitch and yaw are shown in figure 8(B–D). There is an evident periodic variation in the roll angle that increases with the fin frequency. In figure 8(D), we observe that the yaw angles for both frequencies can keep fairly stable (approximately 12s for 1 Hz) before starting to drift.

Volumetric PIV

The 3D flow measurements using volumetric PIV are shown for forward swimming (figure 9(A)) and hovering (figure 9(B)). The inset of each panel shows the relationship between the measurement volume and the robotic device. The streamlines are colored by the magnitude of velocity. The iso-surface of vorticity is shown with a translucent gray surface. The flow fields are shown from the bottom view for the forward swimming and the side view for hovering. Movies S6 and S7 show the time evolution of the flow structures during forward swimming and hovering, respectively. For forward swimming, it can be observed that the formation of a vortex tube is generated by the lateral and downward jet associated with the undulating fin

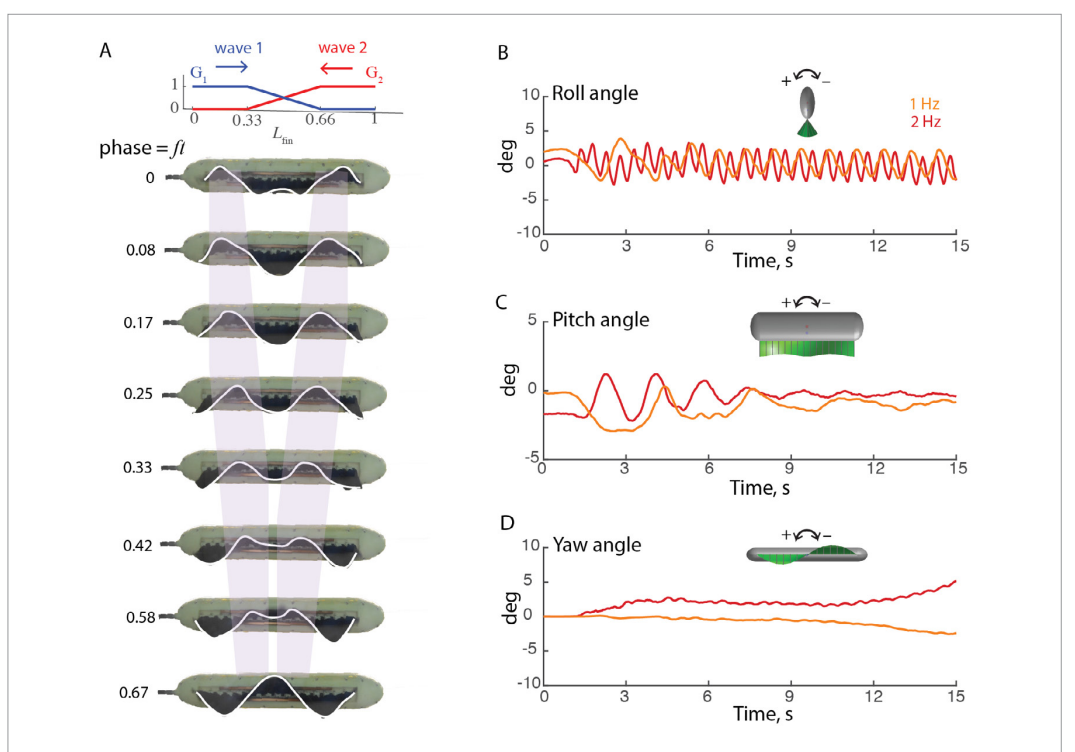


Figure 8. Snapshots of hovering maneuver and time evolution results of the Euler angles. (A) Bottom view showing the peaks of two counter-propagating waves traveling towards the center of the fin (nodal point) at 1.0 Hz. The inset shows the shape control functions G_1 and G_2 . (B) and (D) The time evolution results of roll, pitch and yaw during the hovering motion. See supplementary material movie S5 for the corresponding video.

kinematics. The jet seems to have a stronger velocity magnitude around the center of the jet and the velocity magnitude decays away from the central jet until the streamlines curl around the vortex tube (shown in translucent gray figure 9). It is expected that this lateral jet will change direction from starboard and port sides as the fin undulates. Figure 9(B) show the streamlines and vortex structure during the hovering maneuver with counter-propagating waves. In this case, the streamlines are predominately vertically downward with the tip vortex shed from the fin edge. Although the counter-propagating wave creates a strong downward jet, the velocity magnitude oscillates as the fin undulates (see supplementary movie 6).

Discussion

Swimming maneuvers

Although the versatile maneuver capabilities of ribbon-fin based propulsion have been observed and documented in live animals [8, 19], it has not been demonstrated in free-swimming underwater vehicles. Here a novel robotic vessel with a single undulating fin is used to demonstrate the potential maneuvers of this propulsion mechanism.

For forward swimming, we observe that the swimming velocity increases linearly at low frequencies until the swimming velocity starts to increase at a lower pace compared to the fin frequency. It was also found that the swimming velocity and Euler orientation angles

in forward swimming exhibit smaller standard deviations for the scenarios with two undulations, suggesting that with higher number of undulations along the fin, the motion becomes steadier.

It is observed that the swimming speed depends on the traveling wave speed, $V_{wave} = f\lambda$. Thus, the swimming speed depends on both the frequency and wavelength. Using a runner as an analogy, the speed depends on the length strike and the frequency of each stroke. In a similar fashion, the swimming speed of a swimmer with an undulating fin depends on the wavelength (analogous to the length strike) and the frequency of the traveling wave. The swimming speed exhibits an almost linear relationship with the traveling wave speed. Therefore, a speed control of the vessel could be implemented depending on the traveling wave velocity. On the other hand, the power consumption increases exponentially with the swimming speed.

As to the reversed swimming maneuver, the robotic device is capable of changing direction from forward to backward swimming by changing the direction of the traveling wave without the need to turn. Knifefish are capable of switching swimming directions in a similar fashion at a fraction of seconds during prey capture [12]. Our results of reversed maneuver show that the rapid reversal transition can lead to sharp jumps of the Euler angles, especially prominent for roll and pitch. It is possible that active control of pectoral fins could be used to decrease the changes in the orientation angles of the fish or robotic vessel. When

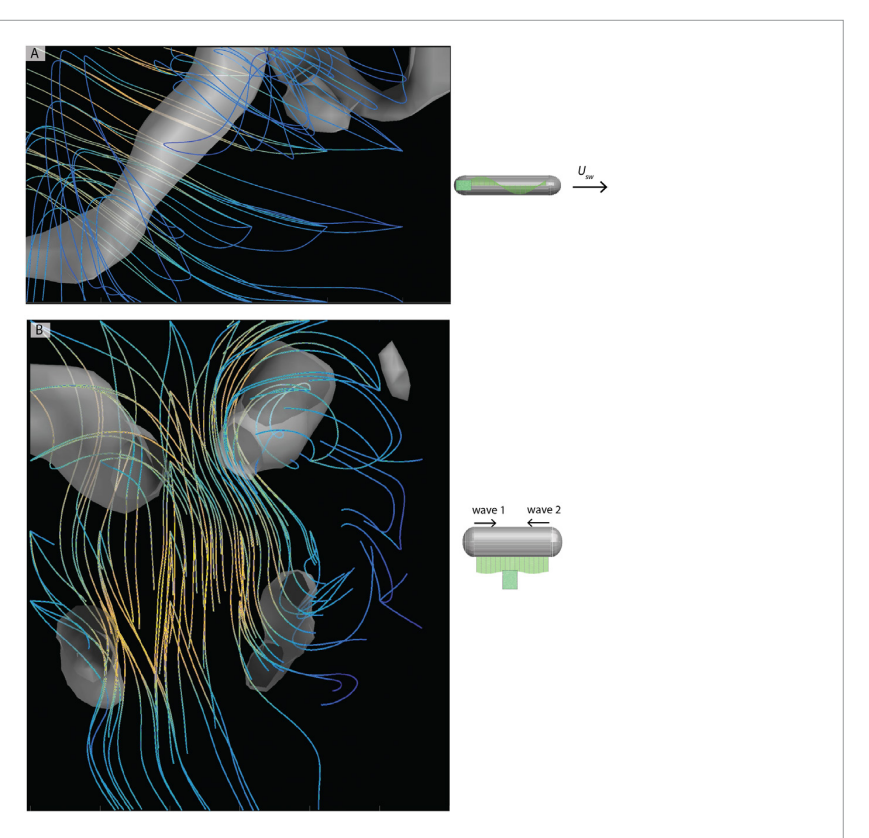


Figure 9. Volumetric PIV (V3V PIV) for forward swimming (A) and station-keeping (B). (A) Streamlines and vortex structures from bottom view during forward swimming at 2.0 Hz with one undulation. The streamlines are color-coded by the magnitude of the velocity. The inset on the right of each panel displays the perspective and location of the laser volume (the green region) with respect to the robot. (B) Flow features generated by the counter-propagating waves along the fin during the hovering maneuver at 2.0 Hz from the lateral view. See supplementary material movie S6 (forward swimming) and S7 (station-keeping) for the flow structure evolution.

actuated at 2.0 Hz as seen in the supplementary material movie S4, the fluctuation during the reversal transition becomes even more pronounced because of the higher kinematic energy switch. However, after the transition, the robot was able to maintain a fairly constant heading direction. In addition, the mean forward swimming velocity (17.2 cm s⁻¹) was higher than the backward velocity $(-11.4 \,\mathrm{cm \ s^{-1}})$. Two factors are most likely the reason for this difference in velocity. First, the trailing plug and the vacuum plug outside the hull increase the form drag of the vessel when it is swimming backwards. Second, the vertical force generated by the fin has a greater force component against the swimming direction for backward motion since the pitch angle is larger (1.695°) compared to the forward swimming session (0.146°). It is important to notice that the knifefish tends to change frequency and wavelength as it reverses direction. These changes in kinematics could also contribute to stabilizing the changes in the orientation angles.

Station keeping of the *KnifeBot* was achieved by carrying head waves and tail waves proceeding towards each other simultaneously. When the nodal point, where the inward counter-propagating waves meet, is positioned at the midpoint of the fin, the force component along the surge direction cancels while the force

component in the heave direction does not. Previous experimental results [19, 39] have shown that the heave force grows as the frequency rises, which agrees with our observation as the vessel is able to swim in the vertical direction considerably faster when the fin is actuated at 2 Hz ($8.8~{\rm cm~s^{-1}}$) compared to 1 Hz ($2.5~{\rm cm~s^{-1}}$). An appropriate frequency can also be used to maintain a depth where the heave force is equal to the submerge weight. For the current research stage, no feedback control was implemented to maintain the heading direction, therefore any flow disturbance could cause the yaw angle to deviate after a long period of time, as displayed in figure 8(D). Despite this, the robot was able to stay in the case of 1 Hz approximately 12 s without a drift in yaw.

Note on the role of pectoral fins

Knifefish and other ribbon-fin based swimmers tend to modify the pectoral fin configuration at different swimming cruise velocities [18]. These changes are more likely to counterbalance the torque generated by the undulating fin and thus swim in a fixed orientation without rotating. The positive pitching torque generated by the fin is indeed observed in our measurements as the pitch angle increases with the fin frequency (figure 5(B)). However, the torques created

by the buoyancy force and weight around the center of mass can also be used to counterbalance the fin torques to swim without rotation. When the undulating frequency is low (below 1.0 Hz and 1.5 Hz for one and two undulations respectively), the moment generated by the center of mass and center of buoyancy are able to counterbalance the torque from the fin surge force, keeping the pitch angle at zero degrees or below. But for the scenarios at high frequencies, the pectoral fins can play a key role in counterbalancing the torques and achieving stable swimming. Another factor that may also affect results is the body drag force, but its effect is less clear. Also, different fin wave shapes along the fin could be used to modify the torque generated by the fin. Future studies will be focused on investigating the effect of pectoral fin and wave shapes on undulating fin-based propulsion.

Swimming performance and COT

Undulating fin propulsion has been suggested as an efficient propulsion mode for low speed to explore 'complex' environments [8]. However, there has not been experimental data with direct measurement of energy consumption during free-swimming conditions that verify the claim. Korsmeyer et al measured oxygen consumption as a function of swimming speed in two types of swimmers, parrotfish and triggerfish [53]. These fish transit from median or paired-fin (MPF) swimming at low swimming speed to a combination of body-caudal fin (BCF) and MPF at high swimming speed. Their results support the hypothesis that MPF swimming is more efficient than BCF swimming or a combination of BCF and MPF swimming. Even though oxygen consumption can be related to energy expenditure, it is not a direct measurement of energy and the results can be prone to a high level of uncertainty. Although there are many difficulties involved in performing a comparison of the robotic system and a natural swimmer using this propulsion (motor versus muscle efficiency; difference in the elastic properties of the fin membrane and fin rays, difference in kinematics and spacing between rays), the total COT including motor inefficiencies and loss in friction, suggest that the propulsion mechanism is more efficient at low swimming speeds.

Bale *et al* [54] showed that aquatic animals with undulating fin propulsion exhibit an almost constant ratio between the wavelength and the mean amplitude of oscillation of around 20. They called this ratio the optimal specific wavelength (OSW) as it maximizes the propulsive force or swimming speed. Even though this is a significant finding, it is not based on the energy expenditure but on force generation and swimming speed. Moreover, this quantity does not provide insight on the optimal frequency for a specific wavelength. If we use the specific wavelength for our experiments, $SW = \lambda/(h_{\rm fin} \sin{(\theta_{\rm max})}/2)$, the SW is equal to 9.1 and 18.3 for one and two undulations, respectively. The minimum COT found in the robotic

vessel results is in agreement with the findings of Bale et al, as the SW = 18.3 (two undulations) is more efficient based on the COT compared to the SW = 9.1 (one undulation). However, the difference between the COT could greatly change depending on the fin frequency. For example, the difference in the COT between SW = 18.3 and 9.1 at 1.0 Hz is approximately 1.5 J m⁻¹ while at 2.0 Hz, it is 0.4 J m⁻¹.

Another interesting result is the difference of optimal operation between wave efficiency and COT. While the COT indicates a better performance for two undulations (SW = 18.4) at 1.0 Hz, the wave efficiency (i.e. the ratio between swimming speed and wave speed) shows a better performance for one undulation (SW = 9.1) at 1.0 Hz but with a similar performance (plateau-like region) from 1.0 Hz to 2.5 Hz. This highlights some of the limitations of using only the wave efficiency as a metric to evaluate swimming efficiency: it only relates fin kinematics to swimming speed without information of how much energy is needed to generate the motion. Thus, a better wave efficiency is not necessarily the best COT, in particular across different wavelengths. One possible explanation between the difference in wave efficiency and COT performance is that as the wavelength decreases (more number of undulations are present along the fin), the phase difference between each ray is larger. Even though some of the energy to stretch the membrane will be recovered as the membrane 'un-stretched', some energy will be lost due to irreversibility in the process. Therefore, while wave efficiency can provide some useful information about the performance of undulating fin swimming, it poses some clear limitations that should be considered when it is used to evaluate swimming efficiency.

Flow structures

The hydrodynamics of undulating fin propulsion are key to understanding its motion capabilities. Recent studies using a combination of computational fluid dynamics (CFD) simulations and PIV on robotic devices have helped us to understand the intricate fluid structures around undulating fins. For example, Shirgaonkar et al examined the hydrodynamics of a non-translating undulating fin using CFD and PIV results [45]. Curet et al showed the flow structure of counter propagating in undulating fins similar to the wave used by the knifefish during hovering [19]. Neveln et al [42] used a combination of PIV on a robotic device and CFD simulations to analyze the hydrodynamics of cruising ribbon-fin swimmers. They showed that undulating fin swimmers generate an off-axis jet with a series of lined vortex tubes that are shed off the tip edge of the fin. Despite the highly 3D flow structure of undulating fin propulsion, there are no previous experimental 3D flow measurements. The volumetric PIV measurements in this study shed additional light on the flow structure around undulating fins during free-swimming and hovering, and corroborate some previously proposed 3D flow structures [19, 42].

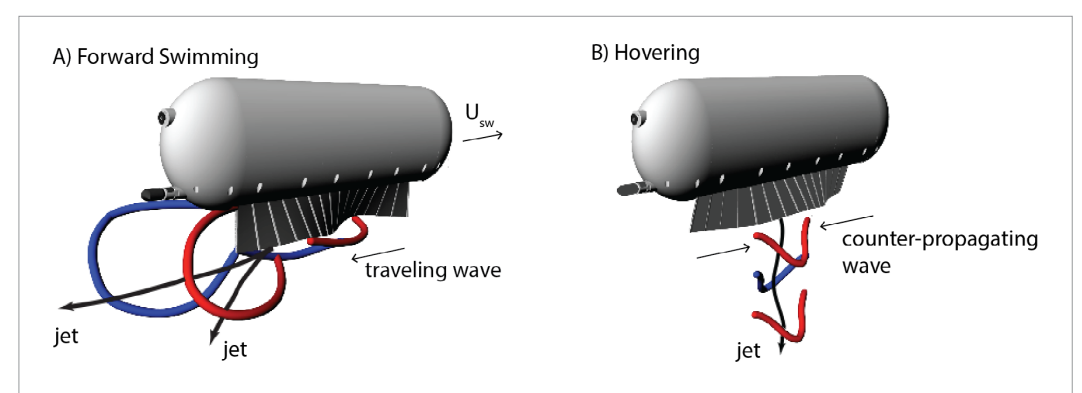


Figure 10. (A) Schematic of 3D vortex structure and flow jet in forward swimming. The vortex tubes are colored to indicate whether they were shed from the left (blue) or right (red) side of the fin. (B) Schematic of vortex tubes and downward jet during hovering.

The volumetric PIV results show an axial jet that has a lateral and downward component as the wave propagates through the fin. The fin kinematics and associated fluid jet form a vortex tube that is shed from the fin (figure 9(A)). The downward jet contributes to the substantial heave force generation while the axial jet component is related to the surge force. For forward swimming, we observed the generation of a tip vortex tube that is shed at the posterior end of the fin. This vortex structure is related to the downward and lateral jet for every half-cycle (figure 9(A)). Although the measurement volume was relatively small, the characteristics of the vortex structure resemble the structure presented by Neveln et al [42], thus providing a validation of such a vortex using experimental 3D flow measurements. A stream-wise jet at an oblique angle to the fin is generated in association with the vortex tubes, which propels the robot forward as well as pitches it up. A schematic of the flow behavior and vortex structure is shown in figure 10(A).

The 3D flow measurements also provide a better picture of the complex flow structure during hovering using counter-propagating waves (figure 9(B)). We observe that the vortex tubes generated by the fin are shed-off at the mid-section of the fin. This vortex structure is associated with a 'pulsed' jet that is pointing downward and lateral with respect to the fin length. Due to the limitation of the measurement volume, we do not observe the complete vortex tube, as it appears to be disconnected at the center. However, we expect that this is a continuous vortex structure that sheds off at the mid-section of the fin while most likely staying attached at the posterior and anterior segment of the fin. A schematic of the proposed vortex structure is depicted in figure 10(B). This downward jet provides a substantial heave force for the robot to swim vertically or perform station keeping. Furthermore, we can anticipate that the undulatory fin can control the combination of surge force and heave force by modifying the position of the nodal point to achieve complex maneuvers. For instance, Ruiz-Torres et al [18] observed that knifefish deploy unsymmetrical counter-propagating waves during forward swimming at minimal speed. Furthermore, such counterpropagating waves can probably provide more stability and control to allow fine adjustment between positive and negative surge motion [17].

Conclusion

Undulatory fin-based propulsion has remarkable locomotion capabilities, as has been documented in live animals studies [11, 18]. Even though there has been considerable progress in understanding the mechanics of this propulsion method [17, 19, 39-45, 54], details regarding the performance and maneuver characteristics of a free-swimming physical model for different fin kinematics have not been investigated before. Toward that end, a novel biomimetic vessel with a single undulating fin running along the length of the robot was developed to control both forward motion and directional maneuvers. The robotic vessel has a slender 3D-printed hull with 16 DC motors, 2 Li-ion batteries and electronic boards with power and orientation sensors encapsulated inside the vessel, enabling free-swimming maneuvers. Different maneuvers including forward swimming (figure 4), diving (figure 4(F)), reversed motion (figure 7), station keeping (figure 8) and vertical swimming (movie S5) were successfully replicated using different fin kinematics. In particular, we examined the swimming performance for forward swimming comparing the efficiency with three different metrics: Strouhal number, wave efficiency and COT. The vessel achieves a Strouhal number, $St = fA/U_{sw}$, in the range of approximately 0.2-0.4 depending on the actuation parameters similar to optimal animal locomotion [47, 57]. The COT (the energy spent per distance travelled) exhibits a V-shape trend with the lowest or optimal performance at low swimming velocity. The robotic device can achieve wave efficiency in the range of 0.35-0.6.

It was observed that increasing the number of undulations helps the robot swim more stably. In the reversed maneuver, the rapid reversal transition introduces a drastic fluctuation of the orientation angles before reaching stable swimming. Station-keeping and vertical swimming were performed by counterpropagating waves along the fin. Using volumetric PIV, we observed the generation of vortex tubes associated with downstream jets directed in both lateral and heave directions for forward swimming. In the hovering maneuver, the counter-propagating waves generate a strong vertically downward jet with the tip vortex shed from the fin edge at some angle. These findings corroborate and clarify 3D flow structures during forward swimming and station-keeping maneuvers using an undulating fin.

Bio-inspired undulating fin propulsion can provide multiple advantages for underwater vessels. Some of the potential advantages are: superior maneuverability to control forward motion and a directional maneuver with a single flexible fin; precise maneuvers suitable for station-keeping and maneuvers in tight spaces; high efficiency at low-speed; reduction of risk in terms of getting tangled in marine plants and ropes, and less impact on the marine ecosystem. Although there is much more to be done regarding the control model of the propulsion system, there is enormous potential in undulating fin propulsion for underwater robotics to the oceanographic, defense and other marine-based industries.

Acknowledgments

This material is based upon work supported by the National Science Foundation under Grant No. 1751548 (NSF CAREER Award from the Division of Civil, Mechanical and Manufacturing Innovation) to O M C and the Office of Naval Research for the acquisition of a Volumetric PIV system (award number N00014-16-1-2505). We thank Edward Henderson, who collaborated in the design of the electronic boards, and Fuxian Gong for her tremendous help in conducting the experiments. We also thank Dan Troolin, Ruben Hortensius from TSI and Amirkhosro Kazemi for their help in conducting volumetric PIV measurements.

ORCID iDs

Oscar Curet https://orcid.org/0000-0002-3202-6841

References

- [1] Yuh J 2000 Design and control of autonomous underwater robots: a survey *Auton. Robots* 8 7–24
- [2] Blidberg D R 2001 The development of autonomous underwater vehicles (AUV); a brief summary *IEEE ICRA* 4
- [3] MacIver M A, Fontaine E and Burdick J W 2004 Designing future underwater vehicles: principles and mechanisms of the weakly electric fish IEEE J. Ocean. Eng. 29 651–9
- [4] Sfakiotakis M, Fasoulas J, Kavoussanos M M and Arapis M 2015 Experimental investigation and propulsion control for a bio-inspired robotic undulatory fin Robotica 33 1062–84
- [5] Bandyopadhyay P R 2005 Trends in biorobotic autonomous undersea vehicles IEEE J. Ocean. Eng. 30 109–39

- [6] Jagnandan K and Sanford C P 2013 Kinematics of ribbon-fin locomotion in the bowfin, Amia calva J. Exp. Zool. A 319 569– 83
- [7] Near T J et al 2012 Resolution of ray-finned fish phylogeny and timing of diversification *Proc. Natl Acad. Sci.* **109** 13698–703
- [8] Blake R W 1983 Swimming in the electric eels and knifefishes Can. J. Zool. 61 1432–41
- [9] Lighthill J and Blake R 1990 Biofluiddynamics of balistiform and gymnotiform locomotion. Part 1. Biological background, and analysis by elongated-body theory J. Fluid Mech. 212 183– 207
- [10] Albert J S 2001 Species Diversity and Phylogenetic Systematics of American Knifefishes (Gymnotiformes, Teleostei) (Ann Arbor, MI: University of Michigan Press)
- [11] Youngerman E D, Flammang B E and Lauder G V 2014 Locomotion of free-swimming ghost knifefish: anal fin kinematics during four behaviors Zoology 117 337–48
- [12] Maciver M A, Sharabash N M and Nelson M E 2001 Preycapture behavior in gymnotid electric fish: motion analysis and effects of water conductivity J. Exp. Biol. 204 543–57
- [13] Snyder J B, Nelson M E, Burdick J W and MacIver M A 2007 Omnidirectional sensory and motor volumes in electric fish PLoS Biol. 5 e301
- [14] Lannoo M J and Lannoo S J 1993 Why do electric fishes swim backwards? An hypothesis based on gymnotiform foraging behavior interpreted through sensory constraints *Environ*. *Biol. Fishes* 36 157–65
- [15] Nelson M E and Maciver M A 1999 Prey capture in the weakly electric fish Apteronotus albifrons: sensory acquisition strategies and electrosensory consequences J. Exp. Biol. 202 1195–203
- [16] Nanjappa P, Brand L and Lannoo M J 2000 Swimming patterns associated with foraging in phylogenetically and ecologically diverse American weakly electric teleosts (Gymnotiformes) Environ. Biol. Fishes 58 97–104
- [17] Sefati S, Neveln I, MacIver M A, Fortune E S and Cowan N J 2012 Counter-propagating waves enhance maneuverability and stability: a bio-inspired strategy for robotic ribbon-fin propulsion Biomedical Robotics and Biomechatronics (BioRob), 2012 4th IEEE RAS & EMBS International Conference (IEEE) pp 1620–5
- [18] Ruiz-Torres R, Curet O M, Lauder G V and MacIver M A 2013 Kinematics of the ribbon fin in hovering and swimming of the electric ghost knifefish J. Exp. Biol. 216 823–34
- [19] Curet O M, Patankar N A, Lauder G V and MacIver M A 2011 Aquatic manoeuvering with counter-propagating waves: a novel locomotive strategy I. R. Soc. Interface 8 1041–50
- [20] Xiong G and Lauder G V 2014 Center of mass motion in swimming fish: effects of speed and locomotor mode during undulatory propulsion Zoology 117 269–81
- [21] Lighthill J 1990 Biofluiddynamics of balistiform and gymnotiform locomotion. Part 4. Short-wavelength limitations on momentum enhancement J. Fluid Mech. 213 21–8
- [22] Lighthill J 1990 Biofluiddynamics of balistiform and gymnotiform locomotion. Part 3. Momentum enhancement in the presence of a body of elliptic cross-section J. Fluid Mech. 213 11–20
- [23] Lighthill J 1990 Biofluiddynamics of balistiform and gymnotiform locomotion. Part 2. The pressure distribution arising in two-dimensional irrotational flow from a general symmetrical motion of a flexible flat plate normal to itself J. Fluid Mech. 213 1–10
- [24] Curet O M, AlAli I K, MacIver M A and Patankar N A 2010 A versatile implicit iterative approach for fully resolved simulation of self-propulsion Comput. Methods Appl. Mech. Eng. 199 2417–24
- [25] Shirgaonkar A A, MacIver M A and Patankar N A 2009 A new mathematical formulation and fast algorithm for fully resolved simulation of self-propulsion *J. Comput. Phys.* 228 2366–90
- [26] Zhang Y, Jia L, Zhang S, Yang J and Low K H 2007 Computational research on modular undulating fin for biorobotic underwater propulsor J. Bionic Eng. 4 25–32

- [27] Zhou H, Hu T, Xie H, Zhang D and Shen L 2010 Computational hydrodynamics and statistical modeling on biologically inspired undulating robotic fins: a twodimensional study J. Bionic Eng. 7 66–76
- [28] Lauder G V et al 2011 Robotic models for studying undulatory locomotion in fishes Mar. Technol. Soc. J. 45 41–55
- [29] Triantafyllou M S and Triantafyllou G S 1995 An efficient swimming machine Sci. Am. 272 64–71
- [30] Kato N 2000 Control performance in the horizontal plane of a fish robot with mechanical pectoral fins *IEEE J. Ocean. Eng.* 25 121–9
- [31] Sfakiotakis M, Laue D M and Davies B C 2001 An experimental undulating-fin device using the parallel bellows actuator *Proc.* 2001 ICRA. IEEE Int. Conf. 3 2356–62
- [32] Epstein M, Colgate J E and MacIver M A 2006 Generating thrust with a biologically-inspired robotic ribbon fin *IEEE/RSJ International Conference* (IEEE) pp 2412–7
- [33] Willy A and Low K H 2005 Development and initial experiment of modular undulating fin for untethered biorobotic AUVs Robotics and Biomimetics (ROBIO), 2005 IEEE International Conference (IEEE) pp 45–50
- [34] Long J H et al 2006 Biomimetic evolutionary analysis: testing the adaptive value of vertebrate tail stiffness in autonomous swimming robots J. Exp. Biol. 209 4732–46
- [35] Lauder G V, Anderson E J, Tangorra J and Madden P G 2007 Fish biorobotics: kinematics and hydrodynamics of selfpropulsion J. Exp. Biol. 210 2767–80
- [36] Low K H 2007 Design, development and locomotion control of bio-fish robot with undulating anal fins Int. J. Robot. Autom. 22 88
- [37] Hu T, Shen L, Lin L and Xu H 2009 Biological inspirations, kinematics modeling, mechanism design and experiments on an undulating robotic fin inspired by Gymnarchus niloticus Mech. Mach. Theory 44 633–45
- [38] Liu F, Yang C and Lee K 2010 Hydrodynamic modeling of an undulating fin for robotic fish design *Advanced Intelligent Mechatronics (AIM)*, 2010 IEEE/ASME International Conference (IEEE) pp 55–60
- [39] Curet O M, Patankar N A, Lauder GV and MacIver M A 2011 Mechanical properties of a bio-inspired robotic knifefish with an undulatory propulsor *Bioinspir. Biomim.* 6 026004
- [40] Wen L and Lauder G 2013 Understanding undulatory locomotion in fishes using an inertia-compensated flapping foil robotic device *Bioinspir*. *Biomim*. 8 046013
- [41] Shang L, Wang S, Tan M and Cheng L 2012 Swimming locomotion modeling for biomimetic underwater vehicle with two undulating long-fins Robotica 30 913

- [42] Neveln I D et al 2014 Undulating fins produce off-axis thrust and flow structures J. Exp. Biol. 217 201–13
- [43] Liu H, Taylor B and Curet O 2017 Fin ray stiffness and fin morphology control ribbon-fin-based propulsion Soft Robot. 4 103–16
- [44] Liu H and Curet O 2017 Propulsive performance of an underactuated robotic ribbon fin *Bioinspir. Biomim.* 12 036015
- [45] Shirgaonkar A A, Curet O M, Patankar N A and MacIver M A 2008 The hydrodynamics of ribbon-fin propulsion during impulsive motion J. Exp. Biol. 211 3490–503
- [46] Lauder GV and Tytell E D 2005 Hydrodynamics of undulatory propulsion Fish Physiol. 23 425–68
- [47] Taylor G K, Nudds R L and Thomas A L 2003 Flying and swimming animals cruise at a Strouhal number tuned for high power efficiency Nature 425 707–11
- [48] Maladen R D, Ding Y, Li C and Goldman D I 2009 Undulatory swimming in sand: subsurface locomotion of the sandfish lizard *Science* 325 314–8
- [49] Gillis G B 1998 Environmental effects on undulatory locomotion in the American eel Anguilla rostrata: kinematics in water and on land *I. Exp. Biol.* 201 949–61
- [50] Liao J C, Beal D N, Lauder GV and Triantafyllou M S 2003 Fish exploiting vortices decrease muscle activity Science 302 1566–9
- [51] Liao J C 2004 Neuromuscular control of trout swimming in a vortex street: implications for energy economy during the Karman gait J. Exp. Biol. 207 3495–506
- [52] Bale R, Hao M, Bhalla A P S and Patankar N A 2014 Energy efficiency and allometry of movement of swimming and flying animals *Proc. Natl Acad. Sci.* 111 7517–21
- [53] Korsmeyer K E, Steffensen J F and Herskin J 2002 Energetics of median and paired fin swimming, body and caudal fin swimming, and gait transition in parrotfish (Scarus schlegeli) and triggerfish (Rhinecanthus aculeatus) J. Exp. Biol. 205 1253–63
- [54] Bale R, Neveln I D, Bhalla A P S, MacIver M A and Patankar N A 2015 Convergent evolution of mechanically optimal locomotion in aquatic invertebrates and vertebrates PLoS Biol. 13 e1002123
- [55] Mireles J et al 2011 Analysis of sealing methods for FDMfabricated parts Proc. from Solid Free-Form Fabrication Symp. pp 185–96
- [56] Lauder GV and Madden PG 2006 Learning from fish: kinematics and experimental hydrodynamics for roboticists Int. J. Autom. Comput. 3 325–35
- [57] Saadat M, Fish F E, Domel A G, Di Santo V, Lauder G V and Haj-Hariri H 2017 On the rules for aquatic locomotion *Phys. Rev. Fluids* 2 083102